

Article

Understanding the Formation of Complex Phases: The Case of FeSi₂

Patrice E. A. Turchi ^{1,*}, Volodymyr I. Ivashchenko ², V. I. Shevchenko ², Leonid Gorb ^{3,4}, Jerzy Leszczynski ³ 
and Aurélien Perron ¹ 

¹ Lawrence Livermore National Laboratory, Livermore, CA 94550, USA; perron1@llnl.gov

² Institute for Problems of Material Science, NAS of Ukraine, 03680 Kyiv, Ukraine; volodymyr.ivashchenko@gmail.com (V.I.I.); vishevchenko23@gmail.com (V.I.S.)

³ Department of Chemistry and Biochemistry, Interdisciplinary Center for Nanotoxicity, Jackson State University, Jackson, MS 39217, USA; leonid.gorb@gmail.com (L.G.); jerzy@icnanotox.org (J.L.)

⁴ Badger Technical Services LLC, Vicksburg, MS 39180, USA

* Correspondence: p.turchi@comcast.net

Abstract: One of the fundamental goals of materials science is to understand and predict the formation of complex phases. In this study, FeSi₂ is considered as an illustration of complex phase formation. Although Fe and Si both crystallize with a simple structure, namely, body-centered cubic (bcc A2) and diamond (A4) structures, respectively, it is rather intriguing to note the existence of two complex structures in the Si-rich part of the phase diagram around FeSi₂: α-FeSi₂ at high temperatures (HT) with a slight iron-deficient structure and β-FeSi₂ (also referred to as Fe₃Si₇) at low temperatures (LT). We re-analyze the geometry of these two phases and rely on approximant phases that make the relationship between these two phases simple. To complete the analysis, we also introduce a surrogate of the C16 phase that is observed in FeGe₂. We clearly identify the relationship that exists between these three approximant phases, corroborated by a ground-state analysis of the Ising model for describing ordering that takes place between the transition metal element and the “vacancies”. This work is further supported by ab initio electronic structure calculations based on density functional theory in order to investigate properties and transformation paths. Finally, extension to other alloys, including an entire class of alloys, is discussed.

Keywords: complex alloys; stability; phase transformation; crystallography



Citation: Turchi, P.E.A.; Ivashchenko, V.I.; Shevchenko, V.I.; Gorb, L.; Leszczynski, J.; Perron, A. Understanding the Formation of Complex Phases: The Case of FeSi₂. *Appl. Sci.* **2023**, *13*, 12669. <https://doi.org/10.3390/app132312669>

Academic Editor: Roberto Bergamaschini

Received: 1 July 2023

Revised: 20 October 2023

Accepted: 24 October 2023

Published: 25 November 2023



Copyright: © 2023 by the authors. Licensee MDPI, Basel, Switzerland. This article is an open access article distributed under the terms and conditions of the Creative Commons Attribution (CC BY) license (<https://creativecommons.org/licenses/by/4.0/>).

1. Introduction

Knowledge accumulated over decades of preparation and characterization of a vast number of inorganic compounds has been used to predict new structures, and consequently, new ways of looking at complex structures have emerged. As a general rule, despite the complexity and the incredible stoichiometry of some of these compounds [1,2], simpler structures can be utilized to characterize them. One promising approach that follows Hilbert’s ideas on geometry [3,4] has been to describe them in terms of polyhedral packing, and this has given rise to various topological approaches [2,5–8]. However, defects, which are so important to understanding the formation of many of these structures, are not yet fully appreciated. One other class of approaches used to confirm and predict the formation of a complex structure (i.e., for specific chemical composition, temperature, and pressure, and possibly other external variables for which a structure displays the lowest minimum Gibbs energy) is to make use of modern tools based on quantum mechanics and computational optimization that rely on the calculation of Gibbs free energy and the exploration of the energy landscape. Finally, the use of empirical correlations and data mining can be useful to establish structural maps and predict, to some extent, new alloy compositions among structures, being part of the already-existing catalog on which the maps are based.

In this work, we ask the following question: Starting from simple, structure-based pure elements that make up an alloy at a given composition, what is the pathway to a structural transformation that leads to the formation of a complex structure at thermodynamic equilibrium for some specific alloy compositions? To better justify this question, here are some facts: Very often, the mixture between a transition metal (TM) and an *sp*-type element leads to the formation of simple (ordered) phase(s) for TM-rich alloys, whereas complex phases form for *sp*-like element-rich alloys. Note that Zn is not a TM, despite being part of the *d* block.

Examples include Al-Ni, Al-Cu, Cu-Zn, Fe-Zn (not shown here), and Fe-Si, whose assessed phase diagrams are displayed in Figure 1 (Refs. [9–14], respectively).

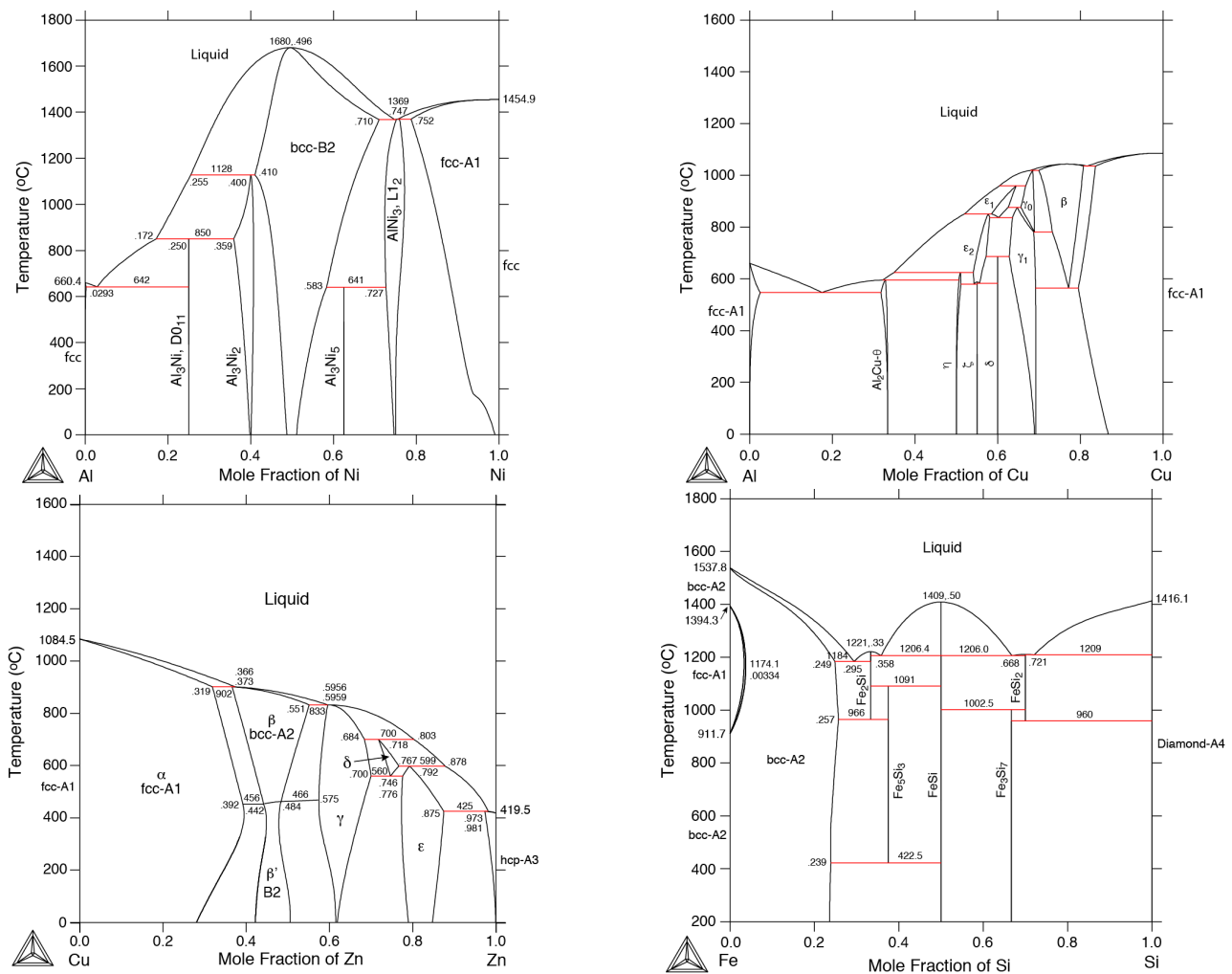


Figure 1. CALPHAD-assessed phase diagrams of Al-Ni, Al-Cu, Cu-Zn, and Fe-Si.

In the case of **Al-Ni**, where both Al and Ni are face-centered cubic (fcc) elements, complex phases are stabilized on the Al-rich side of the diagram beyond a body-centered, cubic (bcc)-based, ordered-phase B2 (CsCl-type, $cP2$, $Pm-3m$) around an equi-atomic composition with two compounds, Al_3Ni ($D0_{11}$, Fe_3C -type, $oP16$, $Pmma$), and Al_3Ni_2 ($D5_{13}$ -type, Al_3Ni_2 -type, $hP5$, $P-3m1$), whereas in the Ni-rich region of the diagram, an fcc-based, ordered-phase $L1_2$ ($L1_2$, $AuCu_3$ -type, $cP4$, $Pm-3m$) forms.

For **Al-Cu**, once again, both of the pure elements exhibit an fcc structure, whereas at least nine complex phases form at various alloy compositions, particularly a tetragonal $\theta-Al_2Cu$ -phase ($CuAl_2$ -type, $tI12$, $I4/mcm$, $C16$) also found in $FeGe_2$.

For **Cu-Zn**, Cu and Zn exhibit fcc and hexagonal close-packed (hcp) structures, respectively, whereas an ordered bcc-based B2 phase forms around the equi-atomic composition,

and three complex phases form in the Zn-rich part of the phase diagram: $D8_2$ - γ (Cu_5Zn_8 -type, $cI52$, $I-43m$), δ ($CuZn_3$ (at HT), $hP3$, $P-6$), and $A3$ - ϵ (Mg-type, $hP2$, $P6_3/mmc$), which is, in fact, based on a distorted hcp structure.

In the case of **Fe-Zn**, the pure elements are based on bcc (low-temperature phase) and hcp structures, respectively, whereas, as a function of alloy composition, four complex phases form: $D8_2$ - Γ (Cu_5Zn_8 -type, $cI52$, $I-43m$), $D8_1$ - Γ_1 (Fe_3Zn_{10} -type, $cF408$, $F-43m$), δ ($hP555$, $P6_3/mc$), and, finally, ζ ($mC28$, $C2/m$).

Finally, in the case of **Fe-Si**, Fe stabilizes with a low-temperature bcc structure, whereas Si has a cubic diamond structure (C-type, $cF8$, $Fd-3m$). As a function of alloy composition, at least four complex phases form in this system: on the Si-rich side of the phase diagram, a semiconducting orthorhombic β - $FeSi_2$ (or Fe_3Si_7 ; LT, $FeSi_2$, $oS48$, $Cmca$, #64) and a metallic tetragonal α - $FeSi_2$ (actually a slightly off-stoichiometric-phase α - Fe_ySi_2 , $y < 1$, with vacancies on the Fe sublattice; HT, $Fe_{0.92}Si_2$, $tP3$, $P4/mmm$, #123) are present in addition to a nearby equiatomic-phase ϵ - $FeSi$ (B20, $cP8$, space group $P2_13$, #198) that is derived from the rock salt structure ($Fm-3m$, $P2_13$, #225). On the Fe-rich side of the diagram, Fe_5Si_3 (Mn_5Si_3 -type, $hP16$, $P6_3/mcm$) and Fe_2Si (Ni_2Al -type, $hP6$, $P-3m1$), and at higher Fe composition (not shown in Figure 1), ordered B2 and $D0_3$ (BiF_3 -type, $cF16$, $Fm-3m$) phases based on the bcc structure are present. For this binary alloy, besides the two forms of $FeSi_2$, it is worth noting the observation of the cubic fluorite γ - $FeSi_2$ phase (C1, CaF_2 -type, space group, $cF12$, $Fm-3m$, #225) that exists in epitaxially stabilized thin-film configuration [15] or as small coherent precipitates [16,17] due to the small misfit to the silicon substrate lattice parameter. This phase will be re-examined in Section 2.

These examples illustrate the fact that, for many TM-X alloys where TM is a *d*-like transition metal element and X is an *sp*-like element (e.g., Al, Ge, Si, Zn, etc.), there is formation of complex phases, especially at X-rich compositions, in contrast to the situation in TM-rich compositions, where simple (ordered) phases tend to form. This would also be the case for, e.g., Cu-Ge, Fe-Ge, and Ti-Al, among many others. Therefore, the question becomes the following: Why is it that, although the pure elements stabilize in a simple structure such as fcc, bcc, or hcp, complex phases form when these elements become constituents of an alloy?

Here, we will focus on the following question: Starting from simple, structure-based pure elements that make up an alloy at a given composition, what is the pathway to a structural transformation that leads to the formation of a complex structure at thermodynamic equilibrium around a specific composition? $FeSi_2$ will be used as a template.

First-principles calculations were used to investigate the stability and the structural, elastic, and electronic properties of β - $FeSi_2$ [18–22], γ - $FeSi_2$ [21,23], and α - $FeSi_2$ [21]. The first-principles approach and the Debye model were combined to predict the vibrational thermodynamic contribution for Fe-Si compounds [24]. In a semi-empirical tight-binding scheme, the total energy and elastic constants of γ - $FeSi_2$ were calculated [25]. This scheme was also employed to (1) investigate the transformation of the electronic structure when the original calcium-fluorite structure is distorted into the orthorhombic one [26], and (2) analyze the leading role of the electron–phonon interaction in promoting the structural distortion from fluorite (γ -) to orthorhombic β - $FeSi_2$ [27]. Semi-empirical tight-binding molecular dynamics simulations were carried out to investigate the γ -to- β structural transformation [23,24], confirming that the driving force leading to the metal–semiconductor structural phase transition originates from a local Jahn–Teller distortion [28,29].

The literature data were analyzed, and it was concluded that the γ -to- β transformation path, the behavior of the $FeSi_2$ phases at high temperatures, their stability, and their thermodynamic and mechanical properties were not yet investigated in the framework of the same first-principles approach. To fill this gap, we will use first-principles calculations that include structural optimization and molecular dynamics to study $FeSi_2$. This will enable us to explain the origin of the intermediate phases that arise during first-principles molecular dynamics (FPMD) simulations of the γ and β phases, to suggest possible mechanisms of

the $\gamma \rightarrow \beta$ and $\beta \rightarrow \alpha$ transformations and to analyze the thermodynamic and mechanical properties of FeSi₂ phases.

The paper is organized as follows. In Section 2, we revisit the crystallography of the two polytype forms of FeSi₂, and define simpler forms (approximants) of these two compounds with their relationships to other possible related phases. In Section 3, we present the details of first-principles calculations. In Section 4, the structural, mechanical, thermodynamic, and electronic structural properties of the α , β , and γ forms of FeSi₂ are presented. Finally, in Section 5, a summary of the present study is discussed.

2. Crystallographic Examination and Relationships

As was said before, there are two polytypes of bulk crystalline iron disilicide (FeSi₂): the semiconducting orthorhombic β -phase (oS48, space group Cmca, #64), stable below $T_C \sim 1275.5$ K (1002.5 °C), and the metallic tetragonal α -phase (tP3, space group P4/mmm, #123; α -Fe_ySi₂, ($y < 1 - \nu$), with vacancy composition, ν , on the Fe sublattice, stable above 1233 K (960 °C) and up to 1484 K (1211 °C), in addition to a nearby equiatomic-phase ϵ -FeSi (cP8, space group P2₁3, #198), stable up to 1682 K (1409 °C). The thermodynamic reactions that take place in the Si-rich part of the phase diagram are:

eutectoid: α -FeSi₂ \rightarrow β -FeSi₂ + Si at 1233 K (960 °C)

peritectoid: ϵ -FeSi + α -FeSi₂ \rightarrow β -FeSi₂ at 1275.5 K (1002.5 °C)

eutectic: liquid \rightarrow α -FeSi₂ + FeSi at 1479 K (1206 °C)

eutectic: liquid \rightarrow α -FeSi₂ + Si at 1482 K (1209 °C)

congruent melting: α -FeSi₂ \rightarrow liquid at 1484 K (1211 °C)

The orthorhombic β -phase has 48 atoms in the unit cell with the following lattice parameters: $a = 9.863$, $b = 7.791$, and $c = 7.833$, in Å [30,31], described in Table 1 with 16 Fe sites and two types of Fe sites (Fe1 and Fe2), and with 32 Si sites with two types of Si sites (Si1 and Si2). This complex structure can be viewed in a first approximation as a stacking of Si-occupied cubes of parameter $a' = a/4$ with an alternate occupation of the cube centers by Fe and vacancy, ν . A detailed description of this structure can be found in Ref. [30].

Table 1. Description of the β -FeSi₂ structure with cell content of $(0\ 0\ 0) + (1/2\ 1/2\ 0)$ and the coordinates of the current (C) structure in units of the lattice parameters a , b , and c of the 24-atom unit cell, and those of the approximant (A) one within the unit cell.

Site		x_C	y_C	z_C	x_A	y_A	z_A
Fe, 8d	Fe1	0.2146	0	0	1/4	0	0
	Fe1	0.7854	0	0	3/4	0	0
	Fe1	0.7146	0	1/2	3/4	0	1/2
	Fe1	0.2854	0	1/2	1/4	0	1/2
Fe, 8f	Fe2	1/2	0.3086	0.1851	1/2	1/4	1/4
	Fe2	0	0.3086	0.3149	0	1/4	1/4
	Fe2	1/2	0.1914	0.6851	1/2	1/4	1/4
	Fe2	0	0.1914	0.8149	0	1/4	3/4
Si, 16g	Si1	0.1282	0.2746	0.0512	1/8	1/4	0
	Si1	0.8718	0.2746	0.0512	7/8	1/4	0
	Si1	0.6282	0.2746	0.4488	5/8	1/4	1/2
	Si1	0.3718	0.2746	0.4488	3/8	1/4	1/2
	Si1	0.1282	0.2254	0.0512	1/8	1/4	1/2
	Si1	0.8718	0.2254	0.0512	7/8	1/4	1/2
	Si1	0.6282	0.2254	0.9488	5/8	1/4	1
	Si1	0.3718	0.2254	0.9488	3/8	1/4	1

Table 1. *Cont.*

Site		x_C	y_C	z_C	x_A	y_A	z_A
Si, 16g	Si2	0.3727	0.0450	0.2261	3/8	0	1/4
	Si2	0.6273	0.0450	0.2261	3/8	0	1/4
	Si2	0.8727	0.0450	0.2739	7/8	0	1/4
	Si2	0.1273	0.0450	0.2739	1/8	0	1/4
	Si2	0.6273	0.04550	0.7261	3/8	1/2	3/4
	Si2	0.3727	0.04550	0.7261	3/8	1/2	3/4
	Si2	0.1273	0.04550	0.7739	1/8	1/2	3/4
	Si2	0.8727	0.04550	0.7739	7/8	1/2	3/4

The tetragonal α -phase has two atoms in the unit cell with the following lattice parameters: $a = 2.7047$, $b = 2.7047$, and $c = 5.1430$, in Å [31–33], described in Table 2 with one Fe site and one Si site. The α -FeSi₂ structure can be viewed as a defected CsCl-type order with alternate layers of Cs (Fe) in the c direction omitted. As a result, the axial ratio $c/2a$ is slightly less than unity, and the Si layers are displaced towards each other. Thus in the [001] direction, the structure is made up of a 4⁴ Fe layer surrounded on either side by 4⁴ Si layers displaced $(a + b)/2$ relative to the Fe layer, giving three-layer units. Fe has eight Si neighbors at a distance of about 2.3 Å, and Si has four Fe neighbors [6]. Note that α -FeSi₂ is a slightly iron-deficient structure and is formed of FeSi₈-joined face-sharing cubes that are very nearly regular (whereas the empty cubes along the c direction, due to Si-Si bonds, are squeezed). On the other hand, in β -FeSi₂, the FeSi₈ cubes that are joined by edge-sharing, as in the fluorite type, are very severely distorted, although the fluorite CaF₂ structure (γ -phase) is still recognizable [30].

Table 2. Description of the α -FeSi₂ structure with the coordinates of the current (C) structure in units of the lattice parameters a and c of the 2-atom unit cell, and those of the approximant (A) structure within the unit cell. \mathcal{V} refers to vacancy.

Site	x_C	y_C	z_C	x_A	y_A	z_A
Fe	0	0	0	0	0	0
Si	1/2	1/2	0.280	1/2	1/2	1/4
\mathcal{V}	1/2	1/2	0.720	0	0	3/4

To complete the list of possible structures at this 1:2 composition, one would have expected to find a similar situation for Fe-Ge. This is not the case; instead, a Θ -FeGe₂ phase (C16, Al₂Cu-type, tI12, I4/mcm, #140) forms, described in Table 3 with 12 atoms in the unit cell [34,35]. Figure 2 shows the three phases described so far.

To define approximants for these three structures, small atomic displacements and local rotations applied to them are required. With the appropriate atomic displacements applied to the different inequivalent sites of the oC48 β -FeSi₂ structure depicted in Figure 2 (such that the coordinates are expressed in units of $n/4$, where n is an integer), one obtains a cubic γ -FeSi₂ CaF₂-type structure, usually defined on an fcc lattice (space group Fm-3m, #225), given in Figure 3.

If the tetragonality of the tP3 α -FeSi₂ structure is ignored and the Si species are located at the center of the cubes, i.e., if the structure is described on a bcc lattice, the resulting arrangement of the three different species (Fe, Si, and vacancies, \mathcal{V}) is given in Figure 3.

Finally, to complete the description, if one applies two so-called clockwise ($z = 1/4$) and anti-clockwise ($z = 3/4$) Hyde rotations on the Archimedean square antiprisms (indicated in Figure 2), where $\tan(\delta) = (1 - 4\alpha)/(2 - 4\alpha)$, with an angle of $\alpha \sim 0.1586$, $\delta \sim 14.987^\circ$, and distance adjustment from $d = (2\alpha^2 - \alpha + 1/4)^{1/2} = 0.37644$ to 0.35355 (with a unit of a), the body-centered tetragonal C16 Θ -CuAl₂-type structure can also be described on an fcc (or a bcc) lattice. Indeed, note that for all three cases, the structural representation can be indeed

described on an fcc or a bcc lattice by considering a Bain transformation [36,37], and the results are shown in Figure 3.

Table 3. Description of the Θ -CuAl₂ structure with the coordinates of the current (C) structure in units of the lattice parameters of the 12-atom unit cell with 8h Al and 4a Cu (with $\alpha = 0.1586$), and those of the approximant (A) structure within the unit cell. \mathcal{V} refers to vacancy.

Site	x_C	y_C	z_C	x_A	y_A	z_A
Cu	0	0	0	0	0	0
Cu	1/2	1/2	0	1/2	1/2	0
Cu	1/2	1/2	1/2	1/2	1/2	1/2
Cu	0	0	1/2	0	0	1/2
Al	α	$1/2 - \alpha$	1/4	1/4	1/4	1/4
Al	$1/2 - \alpha$	$1/2 + \alpha$	1/4	1/4	3/4	1/4
Al	$1/2 - \alpha$	α	1/4	1/4	1/4	1/4
Al	α	$1/2 + \alpha$	3/4	1/4	3/4	3/4
Al	$1 - \alpha$	$1/2 - \alpha$	3/4	3/4	1/4	3/4
Al	$1/2 + \alpha$	$1 - \alpha$	3/4	3/4	3/4	3/4
\mathcal{V}	-	-	-	1/2	0	0
\mathcal{V}	-	-	-	0	1/2	0
\mathcal{V}	-	-	-	1/2	0	1/2
\mathcal{V}	-	-	-	0	1/2	1/2

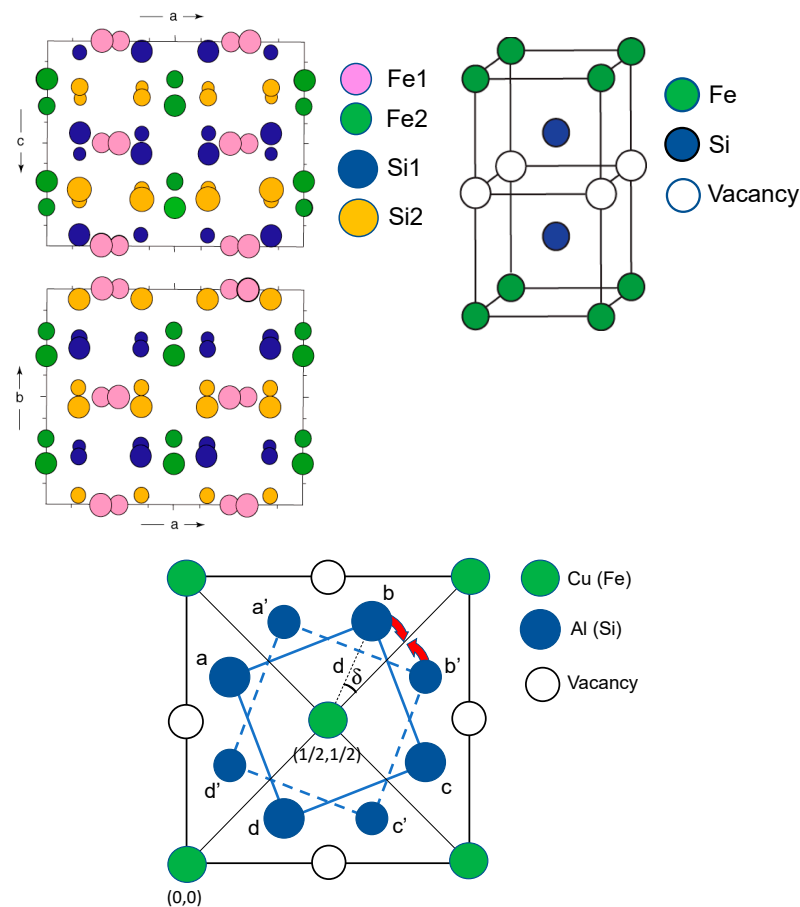


Figure 2. Crystallographic descriptions of β -FeSi₂ (top left), α -FeSi₂ (top right), and Θ -C16 (bottom). (For interpretation of the references to colors in this figure, the reader is referred to the web version of this article).

These three types of ordering on one of the simple cubic sublattices that constitute the bcc lattice (the other simple cubic sublattice is, in the three cases, fully occupied by the

Si species) correspond to three possible ground states on the simple cube at composition $c = 1/2$ for the overall system given by the formula $(\text{TM}_{1-c}\mathcal{V}_c)_4\text{Si}_8$. It is also interesting to note that the three types of chemical arrangements associated with the approximants of $\beta\text{-FeSi}_2$, $\alpha\text{-FeSi}_2$, and Θ can be analyzed as multilayer-type sequencing with one layer of transition metal and one layer of vacancies (\mathcal{V}) along the (110), (001), or (111) direction, respectively, as shown in Figure 3.

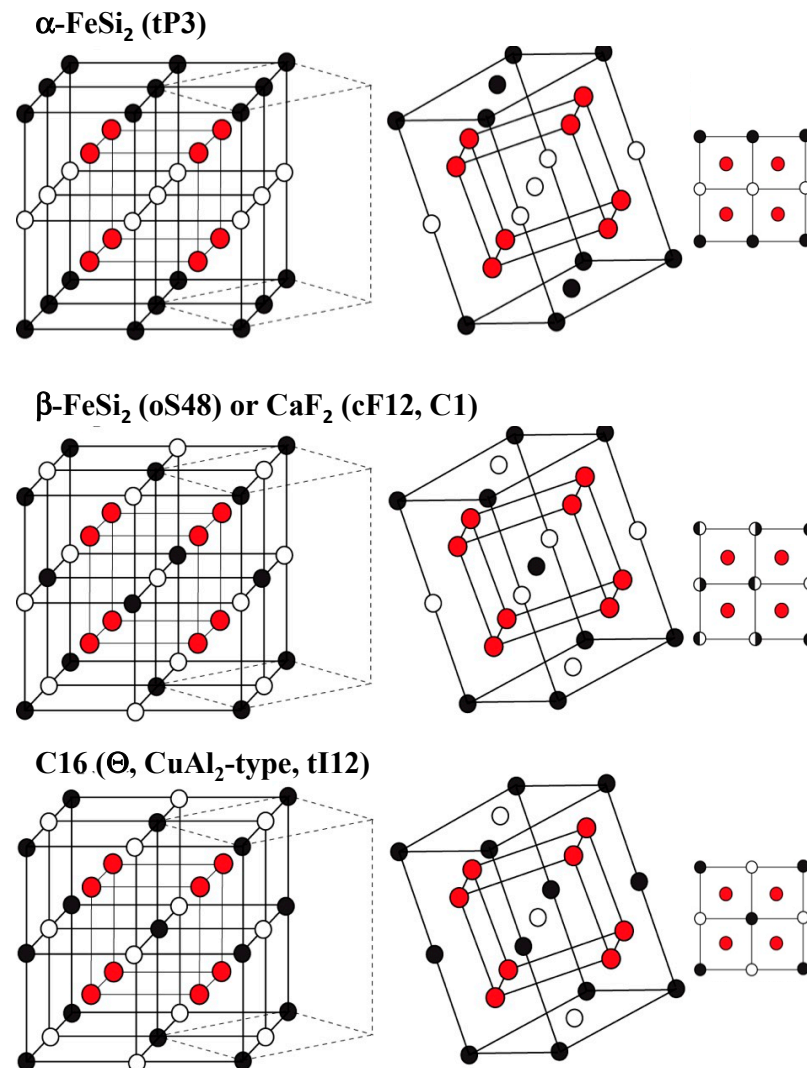


Figure 3. Approximant structures for $\alpha\text{-FeSi}_2$, $\beta\text{-FeSi}_2$, and Θ -C16 (top to bottom order) described on a bcc lattice (left), on an fcc lattice (middle), and with bcc z-axis projection (right). Black (red) circles refer to TM (Si), whereas open circles correspond to vacancies, \mathcal{V} . For the structural representations on the right, half-open half black circles correspond to alternate occupation of TM (or \mathcal{V}) and \mathcal{V} (or TM) along the [001] direction. (For references to colors in this figure, the reader is referred to the web version of this article).

3. Computational Aspects

First-principles calculations of FeSi_2 structures were performed using the quantum ESPRESSO code [38] imposing periodic boundary conditions. Vanderbilt ultra-soft pseudopotentials were used [39], and the generalized gradient approximation (GGA) of Perdew, Burke, and Ernzerhof (PBE) for the exchange-correlation energy and potential [40] was selected. The criterion of convergence for the total energy was 1.36×10^{-6} eV/formula unit. To speed up the convergence, each eigenvalue was convoluted by a Gaussian with a width $\sigma = 0.272$ eV. The cut-off energy was 489.6 eV. Structural optimization was carried out

using the Broyden–Fletcher–Goldfarb–Shanno (BFGS) algorithm [41] by simultaneously relaxing both the cell basis vectors and the atomic coordinates. Structural optimization was considered to be complete when the atomic forces were less than 7 meV/Å, the stresses smaller than 0.05 GPa, and the total energy during the structural optimization iterative process was changed by less than 1.36 meV. Brillouin zone integration was carried out using the Monkhorst–Pack special sets of \mathbf{k} points with (4 4 4), (8 8 6), (8 8 8), and (4 4 8) grids for the 48- and 45-atom supercells, tetragonal 3-atom cell, and 12-atom cubic and monoclinic cells, respectively.

In the first-principles molecular dynamics (FPMD) simulations, we considered the initial 48-atom tetragonal supercells constructed of the tetragonal 6-atom γ - and α -cells via the $(2 \times 2 \times 2)$ translation. One-step FPMD simulations at different temperatures were carried out using the NPT ensemble (constant number of atoms–pressure–temperature). Pressure was applied via the Parrinello and Rahman method [42]. The time step was about 10^{-15} s. The system temperature was kept constant by rescaling the velocity with a tolerance of ± 50 and ± 100 K for low- and high-temperature simulations. All structures reached their time-averaged equilibrium, and afterwards, the total energy and cell volume of the structures fluctuated only slightly around that equilibrium value. The Γ point was used to save computing time without compromising on accuracy. After FPMD simulations, all the structures were relaxed. The β -FeSi₂ structure was generated after FPMD simulations of the 48-atom γ -supercell at 200 K with subsequent relaxation.

The quantum ESPRESSO code was employed to study the phonon spectra of the α - and γ -phases in the framework of the density-functional perturbation theory (DFPT) [43]. The phonon densities of states (PHDOS) of β -FeSi₂ and α -FeSi₂ were determined using the Phonopy code [44]. The elastic moduli were calculated using the ElaStic code [45]. Given the calculated elastic moduli and cell volumes, the fracture toughness was estimated using the procedure described in Ref. [46].

Intermediate phases were identified at certain stages of FPMD simulations. The identification of these structures was carried out via group-theoretical analysis using the “ISOTROPY” code [47] and following the rule discussed in Ref. [48]. The XcrySden code [49] was used to visualize the structures. A detailed description of the applied procedures for the identification of different structures was given in our previous papers [48,50].

4. Results and Discussion

4.1. Ground State Analysis of the Ising Model

Based on the description of the three approximants given in Section 2, ordering processes can be treated as a lattice problem, i.e., in terms of an Ising model on the partially occupied TM- \mathcal{V} sublattice, as was successfully carried out in the case of carbide and nitride compounds [51]. From this point of view, the Si sublattice is ignored in the atomic description of the model. In this Ising model, the configurational (C) part of the energy [52,53] can be written, up to a constant, as:

$$\Delta E^C \sim \frac{1}{2} \sum_R q_R \cdot J_R \quad (1)$$

where J_R is the pair interaction between TM atoms separated by a distance R on the simple cubic lattice, and q_R corresponds to the number of TM atomic pairs. The search for the most stable ordered structures at $T = 0$ K for a finite set of interaction parameters and a given composition reduces to the problem of finding the ground states of this Ising model [52]. This problem has been solved exactly in the case of the simple cubic lattice in the whole range of interaction parameters and composition with first- and second- [54] and up to third-neighbor pair interactions [55]. The results of the analysis are shown in Figure 4, where the ground-state (top) structures are shown together with an ordering map (bottom) that indicates the zones of existence of the various ground states in the space spanned by J_1 and J_2 . Most relevant to this study where the focus is on TMSi₂, i.e., for which the composition is set to the generic composition $(\text{TM}_{1-c}\mathcal{V}_c)_8\text{Si}_8$ with $c = 1/2$, only three ordered

configurations are found, namely, phases IV, V, and VI, that correspond to the approximant of bcc-based β -FeSi₂, α -FeSi₂, and Θ -C16, respectively. It is worth noting that all three ordered structures are fully described with only first- and second-pair interactions.

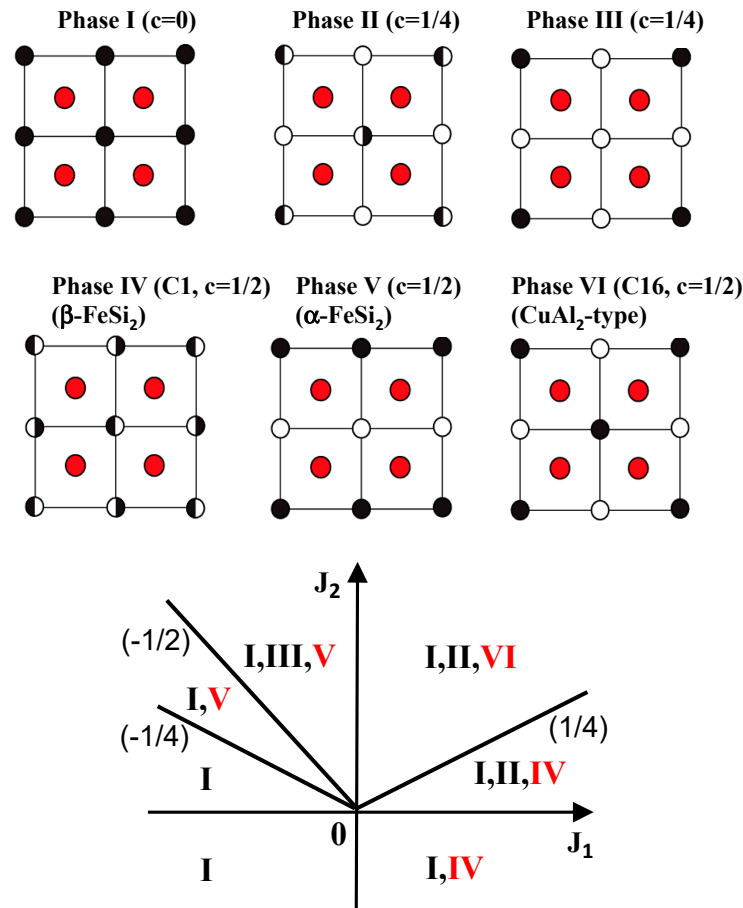


Figure 4. Ground-state (top) structures as obtained from the analysis of the Ising model described with first and second nearest neighbor pair interactions J_1 and J_2 , which are defined for one of the simple cubic (sc) sublattices. This structure analysis applies to the study of the possible ordering between the Fe species (black circles) and the vacancies (open circles, \mathcal{V}) for the alloy of generic composition $(\text{Fe}_{1-c}\text{nc})_8\text{Si}_8$. Phases I, IV, V, and VI refer to B2-FeSi (or pure sc Fe; Segregation), and the bcc-based approximants of β -FeSi₂, α -FeSi₂, and CuAl₂-type (or Θ -C16) of FeSi₂, respectively (see Figure 3). The ordering map (bottom) indicates the zones of existence of the various ground states in the space spanned by J_1 and J_2 (see Equation (1)). The labeling of the sites is given in Figure 3. (For references to colors in this figure, the reader is referred to the web version of this article).

For each position on the $\{J_1, J_2\}$ map, the sequence of ordered structures is indicated within a definite range of composition (here, $c = 0$ (or 1), $1/4$ (or $3/4$), or $1/2$), and for an intermediate composition, a most stable structure is identified as a mixture of these ordered structures. The following are based on the results displayed in Figure 4:

- Phase IV (bcc-based β -FeSi₂ or C1) is found for $J_1 > 0$, $J_2 < 0$ and $J_1 > 0$, $J_2 > 0$, $J_1/J_2 > 1/4$;
- Phase V (bcc-based α -FeSi₂) for $J_1 < 0$, $J_2 > 0$, $2J_2/|J_1| > 4J_2$ and $J_1 < 0$, $J_2 > 0$, $|J_1| > 2J_2$;
- Phase VI (bcc-based Θ -C16) for $J_1 > 0$, $J_2 > 0$, $J_1/J_2 < 4$.

4.2. Structural Properties

In Figure 5, the 48-atom supercells of the β -, γ -, and α -structures of FeSi₂ are displayed in preparation for the electronic structure-based calculations presented below. Besides

the small reshuffle of the atoms inside the γ -unit cell (C1, CaF₂-type) to obtain the atomic configuration of the β -phase, it is worth noting that the creation of antiphase boundaries every two planes along the (100) direction leads to transformation from the approximant α -FeSi₂ to β -FeSi₂, and similarly, the creation of antiphase boundaries along the (011) direction every two planes transforms the approximant β -FeSi₂ in the one of the Θ phase (C16, Al₂Cu-type), as shown in Figure 6. Strong similarities between these three structures are observed despite their original complexity. Below, we will show that $\gamma \leftrightarrow \alpha$ and $\beta \leftrightarrow \alpha$ transformations can also occur through monoclinic-type deformation of the unit cells.

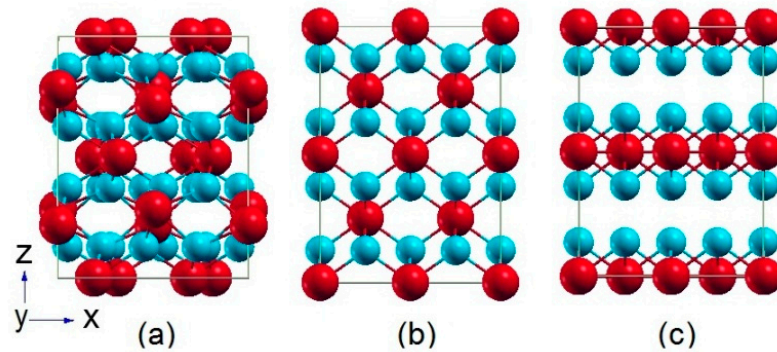


Figure 5. Supercells for the β - (a), γ - (i.e., approximant of γ -FeSi₂) (b), and α - (c) phases. The supercells (a,b) were constructed via the $(2 \times 2 \times 2)$ translation of the corresponding 6-atom tetragonal cells. The large red circles are Fe atoms, and small blue circles are Si atoms. (For interpretation of the references to color in this figure, the reader is referred to the web version of this article).

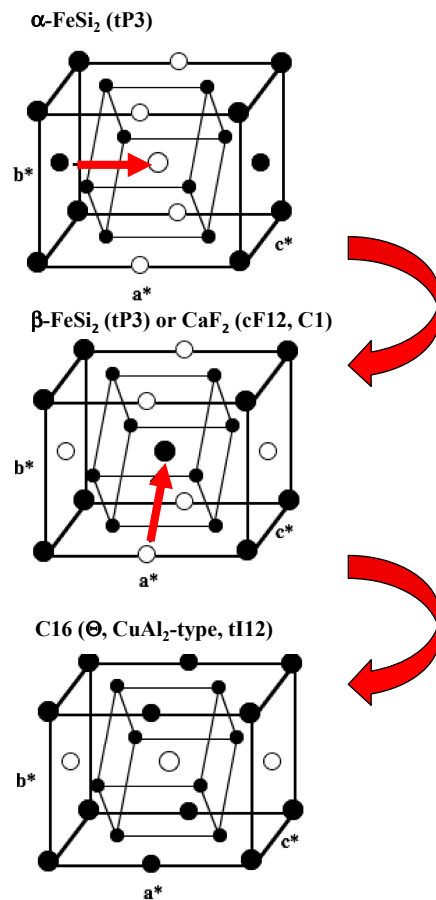


Figure 6. Transformations from α -FeSi₂ to β -FeSi₂ to Θ -C16. Big (small) black circles refer to TM (Si), and open circles to vacancies, V.

4.3. Electronic Structural Properties

For the FeSi₂ phases, the symmetry and the structural and energetic parameters are summarized in Table 4, and the β -structures that were identified during FPMD simulations at 1400 K (β -1400) and 1800-200 K (β -1800) are also included.

Table 4. Symmetry and structural and energetic characteristics of different phases of FeSi₂: N_a is the number of atoms in a unit cell; a, b, and c are the lattice parameters (in Å); V is the cell volume (in Å³/atom); ΔE_T is the total energy (in eV/atom) relative to that of β -FeSi₂. The angles $\alpha = \beta = \gamma = 90^\circ$, except for β -1400 ($\beta = 101.33^\circ$) and β -1800 ($\beta = 111.70^\circ$). The α -Fe_{0.8}Si₂ structure is represented by the 48-atom a-supercell in which three Fe atoms were removed.

Structure	N _a	Symmetry	a (Å)	b (Å)	c (Å)	V (Å ³ /atom)	ΔE_T (eV/atom)
β -FeSi ₂	24	Cmca, #64	9.874 (9.863) ^a (9.869) ^b	7.769 (7.791) ^a (7.774) ^b	7.819 (7.833) ^a (7.846) ^b	12.495 (12.540) ^a (12.540) ^b	0.0000
β -1400	12	C2/m, #12	9.612	7.669	4.068	12.247	0.0357
β -1800	6	C2/m, #12	6.889	3.834	6.520	12.584	0.1064
α -FeSi ₂	3	P4/mmm, #123	2.705 (2.690) ^c (2.710) ^d	2.705 (2.690) ^c (2.710) ^d	5.143 (5.130) ^c (5.140) ^d	12.541 12.374 12.583	0.0564
α -Fe _{0.8} Si ₂	45	P1, #1	2.680	2.680	5.129	12.280*	-
γ -FeSi ₂	3	Fm3m, #225	5.400 (5.400) ^d	5.400 (5.400) ^d	5.400 (5.400) ^d	13.122 (13.122) ^d	0.1743

* The cell volume of the 45-atom cell was divided by 48. ^a Ref [30], experiment; ^b Ref. [22], DFT; ^c Ref. [56], experiment; ^d Ref. [21], DFT.

Figure 7 shows the densities of states (DOS) of different phases of iron disilicide. We compared the calculated DOSs with those reported in other theoretical investigations [21,29] for the stoichiometric α -, β -, and γ -phases, and found that they are in good agreement (not shown here) with those reported here. Our results show that the β -phase is semiconducting, while the γ -phase should display metal conductivity. For β -FeSi₂, the band gap narrows with temperature before its disappearance at T = 1800 K. Both α -FeSi₂ and α -Fe_{0.8}Si₂ exhibit the properties inherent to semimetals.

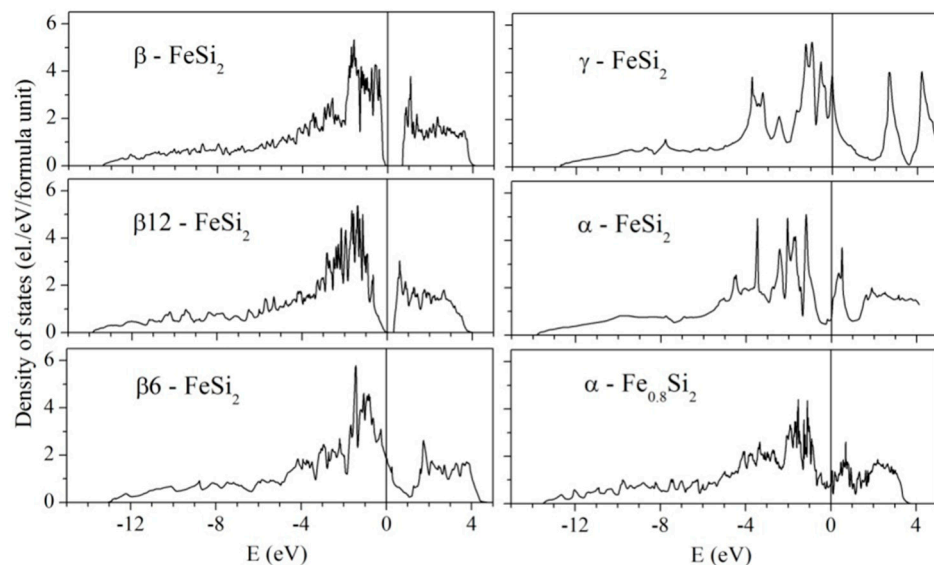


Figure 7. Calculated electronic densities of states for different phases of FeSi₂. The zero of energy corresponds to the Fermi energy. All six phases are described in Table 4, with β 12 \equiv β -1400 and β 6 \equiv β -1800.

Based on these DFT results, total energies versus atomic volume are displayed for β -FeSi₂, α -FeSi₂, and γ -FeSi₂, and their bcc- and fcc-based approximant counterparts in Figure 8. As expected, the stability of FeSi₂ increases from Θ -C16 to α , and to β , which is the ground state at 0 K. Then, the next class of stable structures is bcc based, followed by the class associated with fcc-based structures. This is a posteriori expected, since intrinsically, the two constitutive elements, Fe and Si, have the signature of the bcc phase (and not the fcc one). This result justifies the ground-state analysis of the Ising model discussed in Section 4.1 on the simple cubic lattice, since the other simple cubic lattice is fully occupied by Si atoms and therefore can be ignored in the search for ground-state configurations made of Fe atoms and vacancies.

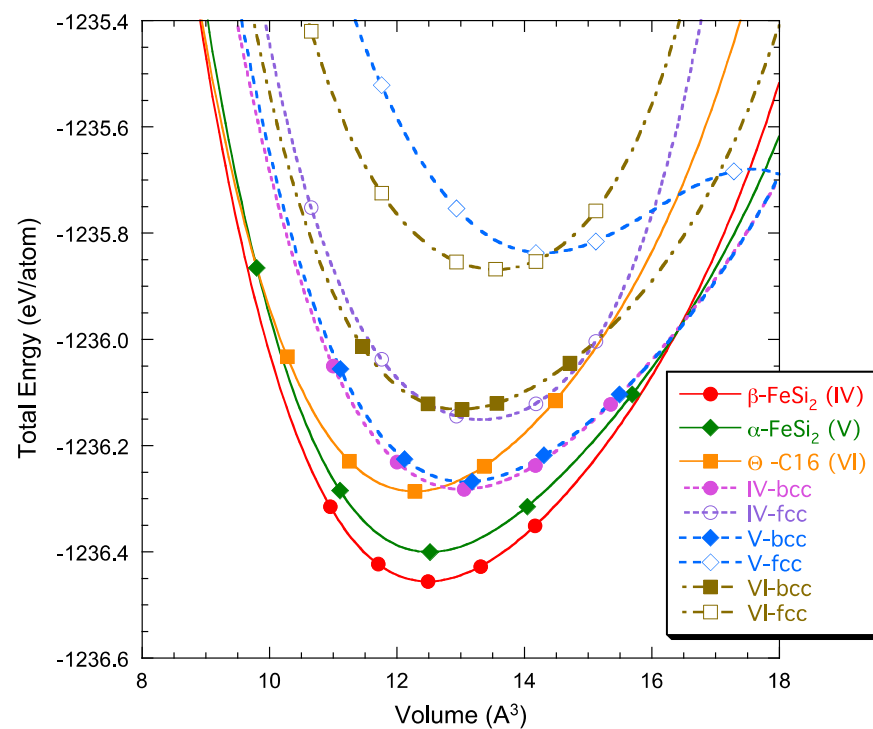


Figure 8. DFT results of total energy (in eV/atom) versus atomic volume in \AA^3 for β -FeSi₂, α -FeSi₂, and Θ -FeSi₂, and their bcc- and fcc-based approximant counterparts. (For interpretation of the references to color in this figure, the reader is referred to the web version of this article).

As shown in Table 4, the calculated lattice parameters for α -Fe_{0.8}Si₂ are closer to those obtained experimentally for the α -phase than the calculated values for α -FeSi₂, which is explained by the fact that the high-temperature α -phase has vacancies primarily located on the Fe sublattice [18,57,58]. The most stable phase among those listed in Table 4 is β -FeSi₂. However, there is an unexpected result: the total energy of the intermediate phase, β -1400, is lower compared to that of the α -phase that was revealed in the experiment at $T > 1240$ K [59]. This fact will be discussed below.

4.4. Mechanical Properties

The calculated Hill elastic moduli, Poisson ratio, and fracture toughness are listed in Table 5 in comparison with those obtained by other authors. A comparison of our data with the few available experimental results shows that good agreement is observed between the calculated and experimental characteristics.

Table 5. Calculated Hill bulk (B), shear (G), and Young (E) moduli (in GPa); Poisson ration (σ); and fracture toughness (K_{IC}) (in $\text{MPa}\cdot\text{m}^{1/2}$) for the α -, β -, and γ -phases of FeSi_2 .

Structure	B	G	E	σ	K_{IC}
β - FeSi_2	180.8 (172.8) ^a	128.1 (130.1) ^a	310.9 (312.0) ^a	0.21 (0.20) ^a	2.3
α - FeSi_2	177.0 (172) ^b	129.4	312.1	0.21	2.3 (2.5) ^d
γ - FeSi_2	173.5 (167) ^b (206) ^c	29.8	84.6	0.42	1.1

^a Ref. [22], DFT; ^b Ref [21], DFT; ^c Ref. [25], theory, tight-binding; ^d Ref. [60], experiment.

Regarding the elastic properties, the small value of G for γ - FeSi_2 indicates that this phase can be unstable against a small shear strain. Given the calculated elastic constants for the orthorhombic β - FeSi_2 phase, the anisotropic factors are estimated [61] for the (100) facet ($A_{100} = 0.960$); for the (010) facet ($A_{010} = 0.943$); and for the (001) facet ($A_{001} = 1.013$). The value $A_i = 1$ suggests completely isotropic properties. In the case of β - FeSi_2 , we observe anisotropy for each facet. Judging from the calculated anisotropic factors, most likely the (010) and (100) facets will be the main sliding planes. Based on the elastic constants, the linear bulk moduli along the different axes were also estimated: along the a-axis, $B_a = 464.8$ GPa; along the b-axis, $B_b = 621.8$ GPa; and along the c-axis, $B_c = 557.9$ GPa. This finding indicates that the compressibility of β - FeSi_2 is anisotropic.

In Table 5, the estimated fracture toughness is presented for the three phases of FeSi_2 in comparison with available experimental values. For α - FeSi_2 , the predicted value is in good agreement with the experiment. The fracture toughness of the γ -phase is the smallest compared to the values of K_{IC} for the α - and β -phases. The latter phases exhibit fracture toughness comparable to that of TiC ($2\text{--}3 \text{ MPa}\cdot\text{m}^{1/2}$) [46].

4.5. Stability and Thermodynamic Properties

To investigate the stability and thermodynamic properties of the α - and β -phases, we calculated their phonon densities of states (PHDOS). Since β - FeSi_2 is a large-unit system, we used, for this purpose, the Phonopy code. The calculated phonon spectrum was compared with that obtained in the theoretical investigation of [24], and we found that they are in good agreement. For α - FeSi_2 , the PHDOS was calculated using the DFPT approach for the 3-atom cell and the Phonopy code for the 48-atom supercells. The results are presented in Figure 9. One can note that, for α - FeSi_2 , both methods provide similar results, and in further investigations, the PHDOSs were calculated using the Phonopy code. The gap between 12 THz and 14.5 THz in the PHDOS of α - FeSi_2 is lacking in the spectrum of the β -phase because of the large number of inequivalent sites with different surroundings.

In Figure 10 the calculated heat capacity as a function of temperature is shown for the β -phase in comparison with the experimental results [62,63]. Although the experimental data are scattered, the calculated curve in the temperature region up to 1000 K reproduces the overall temperature evolution of the experimental $C_v(T)$ rather well. Thus, the simplest model based on phonon spectra is capable of describing the thermodynamic properties of β - FeSi_2 with acceptable accuracy in a temperature range up to 1000 K.

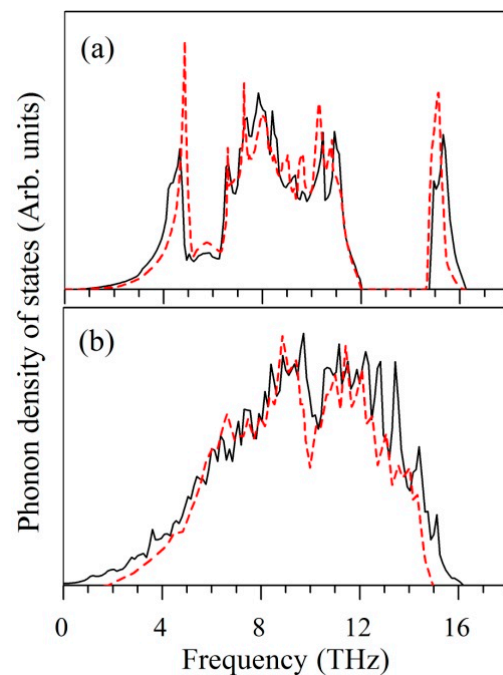


Figure 9. Phonon densities of states (PHDOS) for (a) the α -phase calculated using DFPT (red dashed line) and the Phonopy code (black solid line), and (b) the β -phase calculated using the Phonopy code in the present work (black solid line) and the results of Ref. [24] (red dashed line). (For interpretation of the references to color in this figure legend, the reader is referred to the web version of this article).

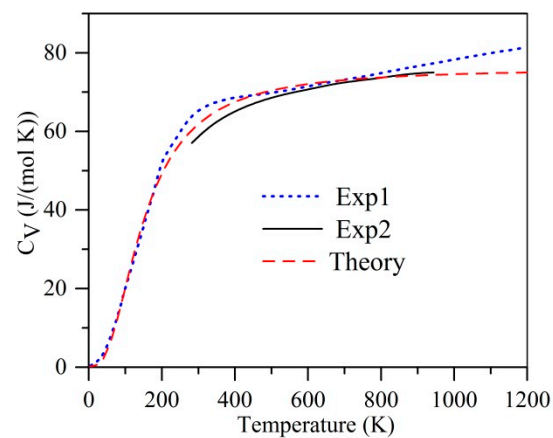


Figure 10. Calculated heat capacity at constant volume (C_V) (red dashed line) for the β -phase in comparison with experimental heat capacity at constant pressure (C_P) determined in Ref. [62] (blue dotted line) and results from Ref. [63] (black solid line). (For interpretation of the references to color in this figure, the reader is referred to the web version of this article).

4.6. Temperature-Induced Phase Transformation in γ -FeSi₂

In this Section, we will consider the temperature-induced phase transformations in γ -FeSi₂, and then, we will describe the possible phase transitions in the β - and α -phases. FPMD simulations were performed for γ -FeSi₂ at different temperatures from 100 K to 2400 K. Using group-theoretical analysis and visualization of the atomic configurations at different stages of the simulations, the possible intermediate and final structures that formed during the simulations at a certain temperature were identified. In Figure 11, the total energy and structural parameters are shown for the 48-atom supercell of γ -FeSi₂ as functions of the time of FPMD simulations (t) at 200 K. For comparison, Figure 11 shows the $E_T(t)$ dependences determined at 600 K and 1400 K. An analysis of the results of the FPMD simulations enabled us to select a time interval between 300 fs and 600 fs, during

which the system reached local stability (“plateau” in the $E_T(t)$ dependences in Figure 11). During this interval, at $T < 800$ K, the γ_1 – γ_3 intermediate structures were identified. A description of the intermediate structures is given in Table 6. One can see from this table that the P-1 (α -Fe_{0.8}Si₂) and C2/m intermediate phases with different numbers of atoms in the unit cell form at temperatures higher than 100 K. The β -phase was the final structure at temperatures up to 400 K and, at $T \geq 400$ K, the final 12-atom C2/m structures (γ_4 , γ_5) formed (cf. Table 6). Note that the P-1 and C2/m space groups are sub-groups of the Fm-3m and Cmca space groups [47]. These results clearly indicate that the intermediate structures are temperature-dependent.

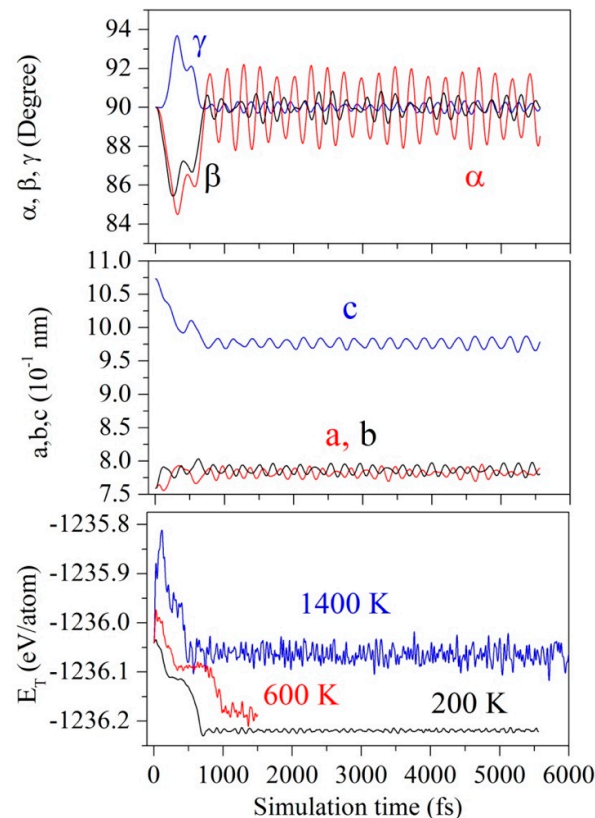


Figure 11. Total energy (E_T) and lattice parameters (a , b , c , α , β , γ) of γ -FeSi₂ as functions of simulation time at 200 K. For comparison, the $E_T(t)$ dependences obtained after FPMD simulations at $T = 600$ K and 1400 K are presented. (For references to colors in this figure, the reader is referred to the web version of this article).

To clarify the possible origin of the identified structures, the phonon spectrum of the γ -phase was investigated. The calculated phonon dispersion curves for γ -FeSi₂ are shown in Figure 12. The points Γ , X, and L and directions Δ , Σ , and Λ in the Brillouin zone are associated with imaginary frequencies of the phonon modes. The phonon modes, such as Γ_{5+} , X_{5-} , L_{3-} , and $\Sigma_{3(1/2\ 1/2\ 0)}$ with imaginary frequencies (cf. Figure 12) could be responsible for the phase transformations in γ -FeSi₂. Here, it should be noted that the semi-empirical phonon spectrum in Ref. [27] also has imaginary frequencies at these points, except at the L point in the present results. In Table 7, the possible structures that could arise due to the softening or condensation of the Γ_{5+} and L_{3-} phonon modes are listed. The Γ_{5+} optic mode was selected, although it has a high real frequency since, at finite temperatures, its softening can cause spontaneous strains and structural changes [47]. The results presented in Table 7 clearly indicate that the direction vector of a phase transition, \mathbf{P} (cf. Refs. [47,48,50] for more details), is very sensitive to temperature and associated with different combinations of phonon modes activated at different temperatures. Here, we note that the formation of the γ_1 and γ_2 phases could only exist because of the monoclinic

strains $\epsilon_{xy} \neq \epsilon_{yz} \neq \epsilon_{xz}$ ($\gamma 1$) and $\epsilon_{xy} \neq \epsilon_{yz} = \epsilon_{xz}$ ($\gamma 2$), since the monoclinic strains have Γ_{5+} symmetry [47]. Indeed, Figure 11 shows that the intermediate-phase $\gamma 2$ forms due to a change in cell angles $\alpha \approx \beta \neq \gamma$ associated with $\epsilon_{xy} \neq \epsilon_{yz} = \epsilon_{xz}$ strains.

Table 6. Structures of the intermediate and final structures identified during FPMD simulations of γ -FeSi₂ at different temperatures (T). The space groups of the identified structures were Fm-3m (γ), P-1 ($\gamma 1$), and C2/m ($\gamma 2$ – $\gamma 5$).

Phase, Temperature (K)	a, b, c (Å)	α β , γ (Degree)	Wyckoff Position
γ T < 100	5.400 5.400 5.400	90.00 90.00 90.00	Fe 1a 0.000 0.000 0.000 Si 2c 0.250 0.250 0.250
$\gamma 1$ 100 ≤ T < 200	3.319 3.523 3.552	94.56 116.79 116.60	Fe 1h 0.500 0.500 0.500 Si 1i 0.003 0.776 0.230
$\gamma 2$ 200 ≤ T < 400	4.731 5.268 3.234	90.00 129.854 90.00	Fe 2d 0.000 0.500 0.500 Si 4g 0.000 0.226 0.000
$\gamma 3$ 400 ≤ T ≤ 800	6.333 3.742 5.974	90.00 118.44 90.00	Fe 4i 0.186 0.000 0.726 Si 4i 0.598 0.000 0.875 Si 4i 0.827 0.000 0.643
$\gamma 4, \gamma 5$ T > 800 K	7.125 9.342 3.756	90.00 100.44 90.00	Fe 4i 0.243 0.000 0.881 Fe 4h 0.000 0.783 0.500 Si 8j 0.278 0.126 0.414 Si 4g 0.000 0.119 0.000 Si 4g 0.000 0.634 0.000

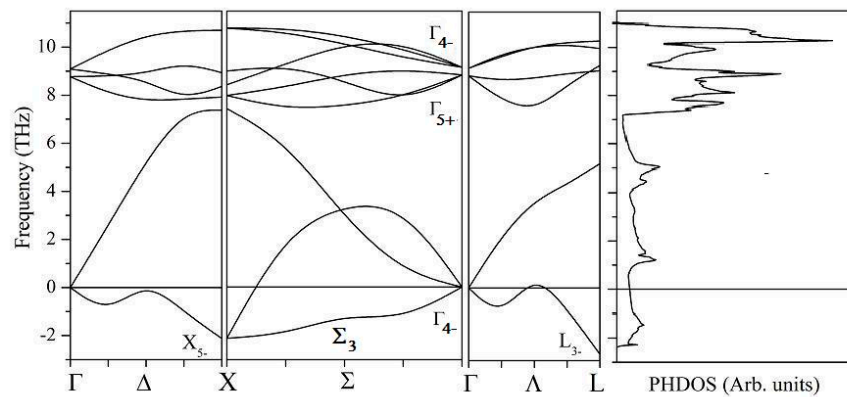


Figure 12. Phonon dispersion curves along symmetric directions for γ -FeSi₂. The negative scale refers to imaginary frequencies.

Table 7. Symmetry, number of atoms in the unit cell (N_a) of the $\gamma 1$ – $\gamma 5$ phases that could form as a result of softening or condensation of the Γ_{5+} and L_{3-} phonon modes coupled to subsequent strains $e_0 = \epsilon_{xx} + \epsilon_{yy} + \epsilon_{zz}$, $e_1 = \epsilon_{xx} + \epsilon_{yy} - 2\epsilon_{zz}$, $e_2 = 3^{1/2}(\epsilon_{xx} - \epsilon_{yy})$, ϵ_{xy} , ϵ_{yz} , ϵ_{xz} according to a direction vector (P) [47].

Phonon Mode	Γ_{5+}			L_{3-}		
	Phase	$\gamma 1$ P-1, #2	$\gamma 2$ C2/m, #12	$\gamma 3$ C2/m, #12	$\gamma 4$ C2/m, #12	$\gamma 5$ C2/m, #12
N_a		1	1	6	12	12
P		S1(a,b,c)	C2(a,a,b)	P2(a,a,000000)	C12(a,b,a,b,0,0,0,0)	C18(a,b,b,a,0,0,0,0)
Strain		$e_0, e_1, e_2,$ $\epsilon_{xy}, \epsilon_{yz}, \epsilon_{xz}$	$e_0, e_1,$ $\epsilon_{xz} + \epsilon_{yz}, \epsilon_{xy}$	$e_0, e_1, e_2,$ $\epsilon_{xz} + \epsilon_{yz}, \epsilon_{xy}$	$e_0, e_1, e_2, \epsilon_{xy}$	$e_0, e_1, -\epsilon_{xz} + \epsilon_{yz}, -\epsilon_{xy}$

As for the X_{5-} phonon mode, it is worth noting that the collapse of the X_{5-} mode could also lead to the formation of 12-atom C2/m structures according to the C15 direction vector [47]; however, it is highly unlikely since the phonon anomaly at the L point is deeper than at the X-point. In Ref. [27], it is assumed that the formation of the β -phase could be due to softening of the optical phonon at the $\Sigma(1/2\ 1/2\ 0)$ point. Indeed, according to our analysis, the γ -to- β transition could be caused by the collapse of the $\Sigma_3(1/2\ 1/2\ 0)$ mode according to the direction vector P5; however, this transition will occur without a coupling to strains [47], which is in contradiction with experiments [57,58,62] and our data. The FPMD simulations of γ -FeSi₂ show that, at $T < 400$ K, the following transformation paths take place: Fm-3m \rightarrow P-1 \rightarrow Cmca and Fm-3m \rightarrow C2/m \rightarrow Cmca. This indicates that the γ -to- β transition that allows the formation of intermediate structures is more favorable than the direct transformation due to softening of the $\Sigma_3(1/2\ 1/2\ 0)$ mode, as in the case of the Fm-3m-to-R-3m transition in B1-SiC [48].

4.7. Structural Transformations in β -FeSi₂ and α -FeSi₂

Now let us return to the analysis of the β -to- α transition. The goal is to understand which of the two scenarios is the most likely—(1) β -FeSi₂ \rightarrow α -FeSi₂, and then, α -FeSi₂ \rightarrow α -Fe_ySi₂ + ϵ -FeSi (direct transition), or (2) β -FeSi₂ \rightarrow α -Fe_ySi₂ + ϵ -FeSi (indirect transition)—since experiments never definitely answered this question [57,58,62]. Hence, the following investigations were carried out. First, the stability of both the β - and α -phases was estimated by comparing their Gibbs free energies; then, the optimum composition of α -Fe_ySi₂ in the reaction α -FeSi₂ \rightarrow α -Fe_ySi₂ + ϵ -FeSi was found, and the γ -phase was shown to possibly transform into the α -phase under strain. Second, FPMD simulations of the β structure at different temperatures up to 2400 K were performed.

The difference in the Gibbs free energies of β -FeSi₂ and α -FeSi₂ (ΔG) as a function of temperature is shown in Figure 13. The calculated transition temperature $T_C = 1825$ K was found to be higher compared to that obtained in the experiment (~ 1240 K) [57,58,62] and in the calculations based on the Debye model (1140 K) [24]. This finding indicates the possibility of a direct β -FeSi₂ \rightarrow α -FeSi₂ transition.

Once it is assumed that the stoichiometric α -FeSi₂ phase could be stabilized at high temperature, let us consider the possibility of its decomposition into ϵ -FeSi and α -Fe_ySi₂ [57,58]. For this purpose, one writes the formation energy of the ϵ -FeSi + α -Fe_ySi₂ system, ΔG , as:

$$\Delta G(y, T) = 1/3 \cdot [x \cdot E_T(\alpha - \text{Fe}_y \mathcal{V}_{1-y} \text{Si}_2) - x \cdot T \cdot \Delta S(\alpha - \text{Fe}_y \mathcal{V}_{1-y} \text{Si}_2) + z \cdot E_T(\epsilon - \text{FeSi}) - E_T(\alpha - \text{FeSi}_2)] \quad (2)$$

where $x = (2 - y)^{-1}$, $z = 2 \cdot (1 - x)$, \mathcal{V} denotes a vacancy on the iron sublattice, E_T is the total energy, and ΔS is the configurational entropy. The α -Fe_y \mathcal{V}_{1-y} Si₂ phases were described based on a 45-atom supercell, in which the vacancies in the Fe sublattice were distributed randomly. The lattice parameter of the cubic eight-atom ϵ -FeSi structure (space group P213 #198) is found to be 4.450 Å, which is very close to the experimental and other theoretical values of 4.489 Å [56] and 4.41–4.47 Å [21], respectively. Expression (2) was derived under the condition that a number of atoms in the system are preserved before and after the structural transformation, and this condition implies that the α -Fe_ySi₂ phase after decomposition should have vacancies on the iron sublattice.

A negative value of ΔG means that α -FeSi₂ will decompose into α -Fe_y \mathcal{V}_{1-y} Si₂ and ϵ -FeSi with the fractions of x and z , respectively. In Figure 14, ΔG is shown as a function of the iron composition in the α -phase at different temperatures. One can see that in the range 800–1000 K, the stoichiometric α -phase should decompose into ϵ -FeSi and α -Fe_y \mathcal{V}_{1-y} Si₂, for $y \sim 0.8$. This finding is in good agreement with the conclusion that, at temperatures higher than 1240 K, two phases, ϵ -FeSi and α -Fe₂Si₅ (α -Fe_{0.8}Si₂, as in our case), form. The decomposition temperature of the stoichiometric α -phase is seen to be lower than the temperature T_C of the β -FeSi₂-to- α -FeSi₂ transformation, indicating that the latter phase transition is unlikely.

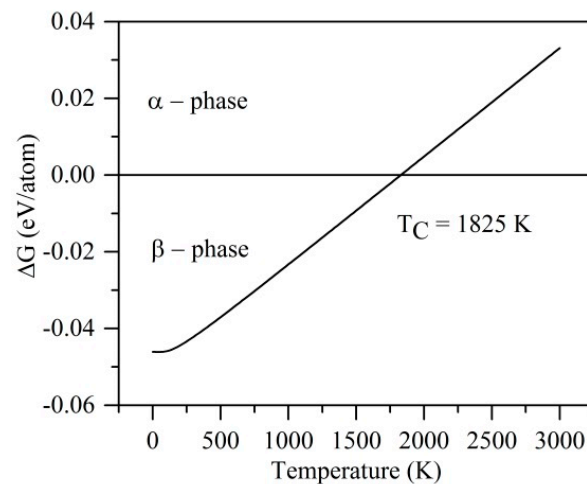


Figure 13. Difference in the Gibbs free energies (ΔG) of the stoichiometric α - and β -phases of FeSi_2 as a function of temperature.

Now let us analyze two possible paths for the $\beta \rightarrow \alpha$ transformation: the diffusion path and the deformation path. For this purpose, we considered the 6-atom fluorite cell (cf. Figure 5b). There are two cases: when the Fe atom in the cell center is moved towards the facet in the z-direction (diffusion path), and when the cell is under monoclinic (100)[001] strain. Both paths lead to the formation of the α -phase, and the energetics of these two paths is shown in Figure 15. It is seen that the deformation path is more energetically favorable than the diffusion one. The $E_T(\epsilon)$ dependence has a local minimum at $\epsilon = 0.5$. All the strained structures have $C2/m$ symmetry.

The possibility of a direct $\beta \rightarrow \alpha$ transition under monoclinic strain of the β -phase is confirmed by the results presented in Figure 16, where the atomic configurations of the strained β -structures are shown. The shear (001)[100] strain, $\epsilon = 1.3$, transforms $\beta\text{-FeSi}_2$ into a distorted $\alpha\text{-FeSi}_2$, and after relaxation, into the perfect α -phase. On the other hand, the $\beta\text{-FeSi}_2$ structure can be formed from $\alpha\text{-FeSi}_2$ under the corresponding monoclinic strain (not shown here).

Finally, attempts were made to promote the transformation of $\beta\text{-FeSi}_2$ into $\alpha\text{-FeSi}_2$ by using FPMD simulations. At different temperatures, a strongly distorted version of the β -phase was revealed. However, at 1400 K, a structural transformation was detected. The total energy and lattice parameters of $\beta\text{-FeSi}_2$ are shown in Figure 17 as a function of simulation time at 1400 K. After about 1500 fs, the system reaches a stable state. This state after relaxation was identified as a 12-atom $C2/m$ structure. A similar six-atom $C2/m$ structure was fixed during simulations at 1800 K and 2000 K. The structures revealed at 1400 K and 1800 K are listed in Tables 4 and 8 as $\beta\text{-1400}$ and $\beta\text{-1800}$. Here, we note one characteristic feature: the structural transformations were accompanied by monoclinic-like strains of the initial unit cells, as in the case of $\beta\text{-FeSi}_2$ (see Section 4.6). For $\gamma\text{-FeSi}_2$, the driving force for the transformations was the softening of the Γ_{5+} and L_3 phonon modes, whereas for $\beta\text{-FeSi}_2$, the transformations occurred due to the anisotropy of the elastic properties of this orthorhombic phase (see Section 4.4).

At $T > 2000$ K, the system has $P1$ symmetry and resembles a melt. It is hard to estimate the melting point in our approach; nevertheless, a temperature of about 2400 K can be estimated, which is much higher than the experimental value of 1453 K. However, this does not come as a surprise since the real structures contain a number of defects that strongly affect (reduce) the melting point. So, it is fair to conclude that we failed in reproducing the β -to- α -phase transition during FPMD simulations at different temperatures; instead, the final structure leads to monoclinic structures. There are two reasons for this. First, the system could reach a local minimum, as shown in Figure 15b, and, second, the indirect transition (see above) $\beta\text{-FeSi}_2 \rightarrow \alpha\text{-Fe}_y\text{Si}_2 + \epsilon\text{-FeSi}$ would be most favorable. Also, we could not transform the α -phase into the β -phase at low temperatures. However, there

is one interesting feature coming out of our FPMD simulations: the β -1400 structure was identified to have lower total energy than for the α -phase (cf. Table 4), and this finding should hopefully encourage researchers to experimentally confirm this phase.

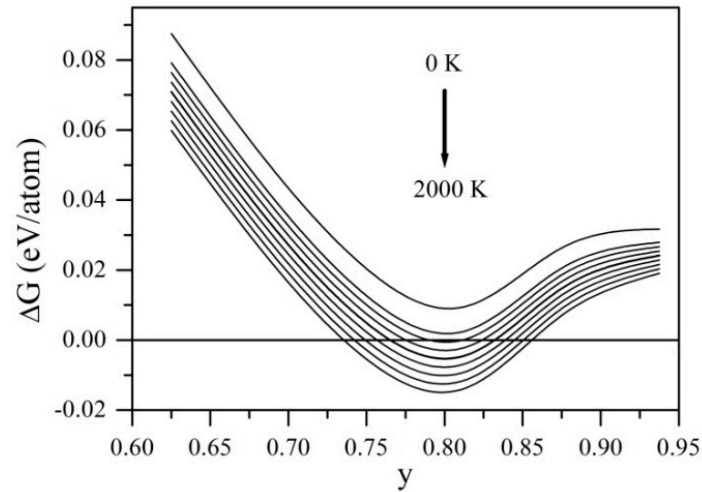


Figure 14. Gibbs free energy differences (ΔG) as functions of y ($\text{Fe}_y\text{V}_{1-y}\text{Si}_2$) for $T = 0, 600\text{--}2000$ K (in step of 200 K), and Cf. expression (2).

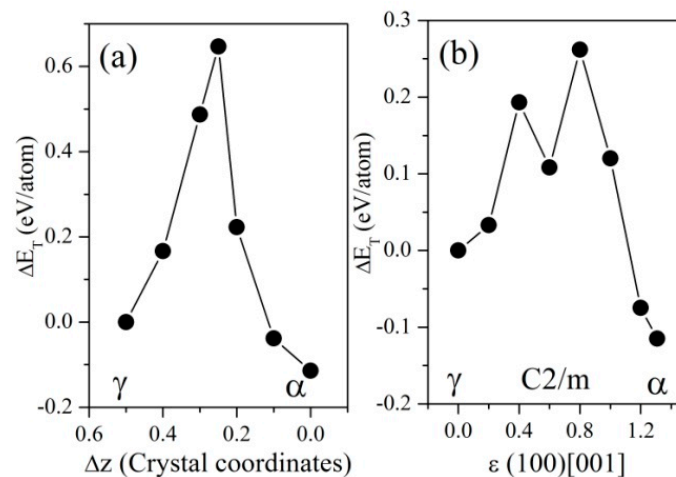


Figure 15. Dependence of the total energy of $\gamma\text{-FeSi}_2$ (ΔE_T) with (a) the shift of the Fe atom from the cell center towards the facet (Δz) (diffusion path), and (b) the shear (100)[001] strain (deformation path).

Thus, extending these results, we conclude that, at high temperature before melting, the system $\alpha\text{-Fe}_y\text{Si}_2 + \epsilon\text{-FeSi}$ is more energetically favorable than the stoichiometric $\alpha\text{-FeSi}_2$ phase. Then, taking into account the results of FPMD simulations, it is suggested that $\beta\text{-FeSi}_2$ should transform according to the deformation path, for example, through twinning. However, at high temperatures, the Fe atoms will diffuse towards the interfaces, promoting the formation of the $\alpha\text{-Fe}_y\text{Si}_2 + \epsilon\text{-FeSi}$ system. Thus $\beta\text{-FeSi}_2$ will transform to $\alpha\text{-Fe}_y\text{Si}_2$ and not to $\alpha\text{-FeSi}_2$. Finally, we note that the suggested mechanism of the β -to- α -phase transition is consistent with the crystallography of the $\beta \leftrightarrow \alpha$ transformation [18].

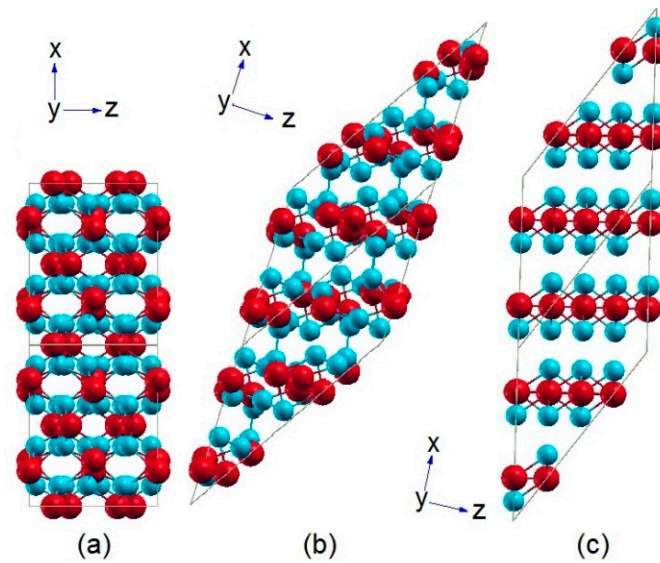


Figure 16. Supercell of β -FeSi₂ translated as $(2 \times 1 \times 1)$: (a) under shear $(001)[100]$ strain, $\varepsilon = 0$; (b) $\varepsilon = 1.3$: unrelaxed structure; and (c) relaxed structure. The color code is similar to the one presented in the caption of Figure 5. (For interpretation of the references to color in this figure legend, the reader is referred to the web version of this article).

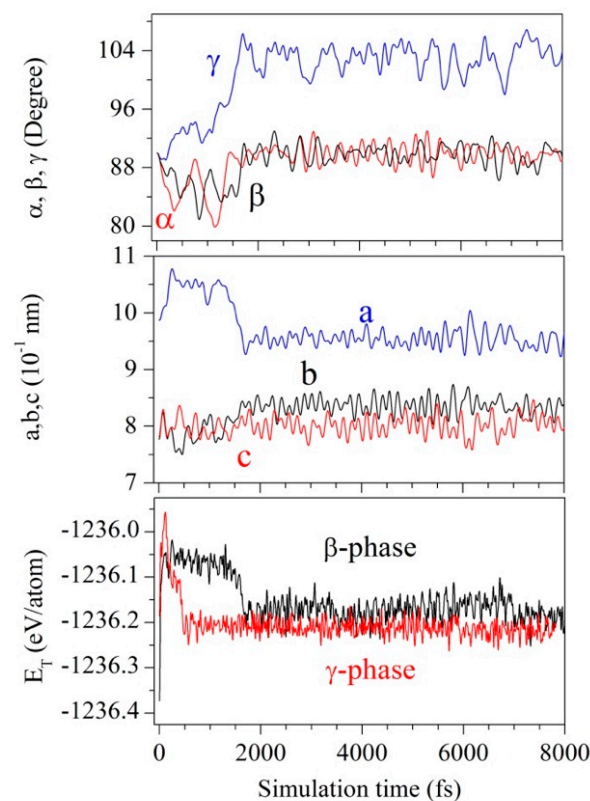


Figure 17. Total energy (E_T) and lattice parameters (a , b , c , α , β , γ) of β -FeSi₂ as functions of simulation time at 1400 K. For comparison, the $E_T(t)$ dependences obtained after FPMD simulations of γ -FeSi₂ at $T = 1400$ K are presented.

Table 8. Structures of the final structures identified during FPMD simulations of β -FeSi₂ at different temperatures (T).

Phase, Symmetry	a, b, c (Å)	α, β, γ (Degree)	Wyckoff Position
γ CmCa	9.874. 7.769. 7.818	90.00, 90.00, 90.00	Fe 8d 0.716 0.000 0.000 Fe 8f 0.000 0.193 0.313 Si 16g 0.128 0.274 0.550 Si 16g 0.373 0.448 0.727
β -1400 C2/m	9.612. 7.669. 4.068	90.00, 101.33, 90.00	Fe 4g 0.000 0.243 0.000 Fe 4i 0.309 0.000 0.646 Si 8j 0.630 0.287 0.546 Si 4i 0.421 0.000 0.203 Si 4i 0.149 0.000 0.059
β -1800 C2/m	6.889. 3.834. 6.520	90.00, 118.70, 90.00	Fe 4i 0.188 0.000 0.721 Si 4i 0.405 0.000 0.126 Si 4i 0.830 0.000 0.644

5. Conclusions

For a broad class of TM-X alloys, where TM is a transition metal and X is an *sp*-type element (such as Al, Si, etc.), alloy formation is insured by substitutional defects for high TM composition, whereas for high X composition, vacancy production is responsible for the formation of usually complex phases, where the complexity is a consequence of atomic relaxations from generally simple structures such as fcc, bcc, or hcp. Hence, FeSi₂, which is the compound we focused on in this work, can be considered not as a binary but as a ternary Fe-Si- \mathcal{V} system. It appears, prior to any quantum mechanical-based analysis, that the bcc-based approximants of the three phases, namely, the orthorhombic β -FeSi₂, the tetragonal α -FeSi₂, and the tetragonal Θ (C16), display ordering between the TM and vacancies, \mathcal{V} , on one of the two simple-cubic sublattices, whereas the other simple-cubic sublattice of the bcc structure is fully occupied by the X (Si) atoms. These three types of ordering are those that result from an “exact” ground-state analysis of the Ising model with a description of the configurational energy defined by first- and second-pair interactions. This study allowed us to energetically locate the three ordered states on an ordering map with constraints on the sign and the amplitude of the first- and second-pair interactions. This work can be used as a tool to design new alloys with specific ordering and also to predict, for example, the transition from the β -FeSi₂ structure to Θ (C16) via the partial substitution of an X species such as Si by Ge. These three approximants are also related via antiphase boundary mechanisms along specific directions, although our first-principles analysis raised questions on this analysis.

First-principles studies that included geometry optimization and molecular dynamics (FPMD) simulations were carried out to investigate the mechanical, electronic, and thermodynamic properties of the β -, α -, and γ -phases of FeSi₂, and also to establish the possible mechanisms of temperature-induced phase transformations among them. One-step molecular dynamics simulations were carried out at different temperatures up to 2400 K. The results showed that the β -phase is semiconducting, while the γ -phases should exhibit metallic conductivity, which is consistent with other experimental and theoretical data. For β -FeSi₂, the band gap narrows with temperature until it disappears at $T \sim 1800$ K. α -Fe_{0.8}Si₂ exhibits properties inherent to semimetals. All the structures under consideration were found to display a low fracture toughness (1.1–2.3 MPa·m^{1/2}) that is comparable to that of TiC (2–3 MPa·m^{1/2}).

A group-theoretical analysis and visualization of the atomic configurations at different stages of simulations allowed us to suggest the possible mechanisms of temperature-induced $\gamma \rightarrow \beta$ and $\beta \rightarrow \alpha$ transformations through the C2/m intermediate states. For γ -FeSi₂, the driving force for the transformations was the structural instability caused by the softening of the Γ_{5+} and L_{3-} phonon modes, whereas for β -FeSi₂, the transforma-

tions occurred due to the isotropy of the elastic properties of this orthorhombic phase. The results of the FPMD simulations showed that the unstable cubic γ -phase transforms into the orthorhombic β -phase at temperatures lower than 400 K, and at $T \geq 400$ K, it transforms into a C2/m structure. The final structures of the FPMD simulations of the β -phase at temperatures up to 2000 K were the 6- and 12-atom C2/m structures. Our results also predict that, at temperatures higher than 800 K, α -FeSi₂ \rightarrow α -Fe_ySi₂ + ϵ -FeSi decomposition should occur with an optimum value of $y = 0.8$. Given these findings, it was suggested that structural transformations in the β -phase should occur via deformation of its unit cell, for example, through twinning, accompanied by the diffusion of the Fe atoms towards interfaces. As a result, the new α -Fe_ySi₂ + ϵ -FeSi system with $y = 0.8$ should be in agreement with the experiments, and this mechanism would not favor direct β -FeSi₂-to- α -FeSi₂ transformation.

Author Contributions: Conceptualization, P.E.A.T.; methodology, P.E.A.T., V.I.I., V.I.S., L.G. and J.L.; formal analysis, P.E.A.T., V.I.I., L.G. and J.L.; investigation, P.E.A.T., V.I.I., V.I.S., L.G. and J.L.; writing—original draft preparation, P.E.A.T., V.I.I., V.I.S., L.G., J.L. and A.P.; writing—review and editing, P.E.A.T. and A.P. All authors have read and agreed to the published version of the manuscript.

Funding: This research received no external funding.

Data Availability Statement: The data presented in this study could be available on request from the corresponding author.

Acknowledgments: The authors are grateful to the directorate of the Summer Institute at Jackson State University, USA, for the opportunity to perform large-scale calculations. Work by A.P. was performed under the auspices of the U.S Department of Energy by Lawrence Livermore National Laboratory (LLNL) under contract DE-AC52-07NA27344 and was supported by the Laboratory Directed Research and Development (LDRD) Program under project tracking code 22-SI-007. LLNL Release No.: LLNL-JRNL-843253.

Conflicts of Interest: The authors declare no conflict of interest.

References

1. Hyde, B.G.; Andersson, S. *Inorganic Crystal Structures*; John Wiley & Sons: New York, NY, USA, 1989.
2. Frank, F.C.; Kasper, J.S. Complex alloys structures regarded as sphere packings. I. Definitions and basic principles. *Acta Cryst.* **1958**, *11*, 184–190. [[CrossRef](#)]
3. Frank, F.C.; Kasper, J.S. Complex alloys structures regarded as sphere packings. II. Classification of representative structures. *Acta Cryst.* **1959**, *12*, 483–499. [[CrossRef](#)]
4. Hilbert, D. *The Foundations of Geometry*, 10th ed.; Open Court: La Salle, IL, USA, 1971.
5. Sinha, A.K. Topologically close-packed structures of transition metal alloys. *Prog. Mater. Sci.* **1972**, *15*, 81–185. [[CrossRef](#)]
6. Pearson, W.B. *The Crystal Chemistry and Physics of Metals and Alloys*; Wiley-Interscience: New York, NY, USA; London, UK; Sydney, Australia; Toronto, ON, Canada, 1972.
7. Szeto, K.Y.; Villain, J. Filling three-dimensional space with tetrahedral: A geometric and crystallographic problem. *Phys. Rev.* **1987**, *36*, 4715–4724. [[CrossRef](#)] [[PubMed](#)]
8. Damasceno, P.F.; Engel, M.; Glotzer, S.C. Predictive self-assembly of polyhedra into complex structures. *Science* **2012**, *337*, 453–457. [[CrossRef](#)] [[PubMed](#)]
9. Ansara, I.; Dupin, N.; Lukas, H.L.; Sundman, B. Thermodynamic assessment of the Al-Ni system. *J. Alloys Compd.* **1997**, *247*, 20–30. [[CrossRef](#)]
10. Chen, H.L.; Du, Y.; Xu, H.; Xiong, W. Experimental investigation and thermodynamic modeling of the ternary Al-Cu-Fe system. *J. Mater. Res.* **2009**, *24*, 3154–3164. [[CrossRef](#)]
11. Liang, S.M.; Schmid-Fetzer, R. Thermodynamic assessment of the Al-Cu-Zn system, part II: Al-Cu binary system. *CALPHAD* **2015**, *51*, 257–260. [[CrossRef](#)]
12. Liang, S.M.; Hsiao, H.M.; Schmid-Fetzer, R. Thermodynamic assessment of the Al-Cu-Zn system, part I: Cu-Zn binary system. *CALPHAD* **2015**, *51*, 224–232. [[CrossRef](#)]
13. Xiong, W.; Kong, Y.; Du, Y.; Liu, Z.K.; Selleby, M.; Sun, W.H. Thermodynamic investigation of the galvanizing systems, I: Refinement of the thermodynamic description for the Fe-Zn system. *CALPHAD* **2009**, *33*, 433–440. [[CrossRef](#)]
14. Lacaze, J.; Sundman, B. An assessment of the Fe-C-Si system. *Met. Trans. A* **1991**, *22*, 2211–2223. [[CrossRef](#)]
15. Onda, N.; Henz, J.; Müller, E.; Mäder, K.; von Känel, H. Epitaxy of fluorite-structure silicides: Metastable cubic FeSi₂ on Si(111). *Appl. Surf. Sci.* **1992**, *56–58*, 421–426. [[CrossRef](#)]

16. Desimoni, J.; Bernas, H.; Behar, M.; Lin, X.W.; Washburn, J.; Liliental-Weber, Z. Ion beam synthesis of cubic FeSi₂. *Appl. Phys. Lett.* **1993**, *62*, 306–308. [[CrossRef](#)]
17. Lin, X.W.; Washburn, J.; Liliental-Weber, Z.; Bernas, H. Coarsening and phase transition of FeSi₂ precipitates in Si. *J. Appl. Phys.* **1994**, *75*, 4686–4694. [[CrossRef](#)]
18. Le Corre, C.; Genin, J.M. Transformation Mechanisms of the $\alpha \leftrightarrow \beta$ Transition in FeSi₂. *Phys. Stat. Sol.* **1972**, *51*, K85–K88. [[CrossRef](#)]
19. Christensen, N.E. Electronic structure of β -FeSi₂. *Phys. Rev. B* **1990**, *42*, 7148–7152. [[CrossRef](#)] [[PubMed](#)]
20. Clark, S.J.; Al-Allak, H.M.; Brand, S.; Abram, R.A. Structure and electronic properties of FeSi₂. *Phys. Rev. B* **1998**, *58*, 10389–10393. [[CrossRef](#)]
21. Moroni, E.G.; Wolf, W.; Hafner, J.; Podloucky, R. Cohesive, structural, and electronic properties of Fe-Si compounds. *Phys. Rev. B* **1999**, *59*, 12860–12871. [[CrossRef](#)]
22. Tani, J.I.; Takahashi, M.; Kido, H. First-principles calculations of the structural and elastic properties of β -FeSi₂ at high-pressure. *Intermetallics* **2010**, *18*, 1222–1227. [[CrossRef](#)]
23. Mäder, K.A.; von Känel, H.; Baldereschi, A. Electronic structure and bonding in epitaxially stabilized cubic iron silicides. *Phys. Rev. B* **1993**, *48*, 4364–4372. [[CrossRef](#)] [[PubMed](#)]
24. Liang, Y.F.; Shang, S.L.; Wang, J.; Wang, Y.; Ye, F.; Lin, J.P.; Liu, Z.K. First-principles calculations of phonon and thermodynamic properties of Fe-Si Compounds. *Intermetallics* **2011**, *19*, 1374–1384. [[CrossRef](#)]
25. Malegori, G.; Miglio, L. Elastic properties of NiSi₂, CoSi₂, and FeSi₂ by tight-binding calculations. *Phys. Rev. B* **1993**, *48*, 9223–9230. [[CrossRef](#)] [[PubMed](#)]
26. Miglio, L.; Malegori, G. Origin and nature of the band gap in β -FeSi₂. *Phys. Rev. B* **1995**, *52*, 1448–1451. [[CrossRef](#)] [[PubMed](#)]
27. Sanguinetti, S.; Calegari, C.; Velasco, V.R.; Benedek, G.; Tavazza, F.; Miglio, L. Phonon mechanism for the orthorhombic distortion in FeSi₂ as compared to cubic CoSi₂. *Phys. Rev. B* **1996**, *54*, 9196–9203. [[CrossRef](#)] [[PubMed](#)]
28. Miglio, L.; Meregalli, V.; Tavazza, F.; Celino, M. Analysis of the metal-semiconductor structural phase transition in FeSi₂ by tight-binding molecular dynamics. *Europhys. Lett.* **1997**, *37*, 415–420. [[CrossRef](#)]
29. Tavazza, F.; Meregalli, V.; Miglio, L.; Celino, M. Assessing the driving force of a structural distortion by the simulated evolution of the local density of states. *Phys. Rev. B* **1999**, *59*, 3480–3488. [[CrossRef](#)]
30. Dusausoy, Y.; Protas, J.; Wandji, R.; Roques, B. Structure cristalline du disiliciure de fer, FeSi₂ β . *Acta Cryst.* **1971**, *27*, 1209–1218. [[CrossRef](#)]
31. Daams, J.L.C.; Villars, P.; van Vucht, J.H.N. *Atlas of Crystal Structure Types for Intermetallic Phases*; ASM International: Materials Park, OH, USA, 1991.
32. Sidorenko, F.A.; Gel'd, P.V.; Dubrovskaya, L.B. Nature of the phase of the Fe-Si system. *Fizika Metallo I Metalloved.* **1959**, *8*, 735.
33. Sidorenko, F.A.; Gel'd, P.V.; Shumilov, M.A. Study of the transformations of a-lebeauite. *Fizika Metallo I Metalloved.* **1960**, *9*, 861–867.
34. Meetsma, A.; de Boer, J.L.; van Smaalen, S. Refinement of the crystal structure of tetragonal Al₂Cu. *J. Solid State Chem.* **1989**, *83*, 370–372. [[CrossRef](#)]
35. Grin, Y.; Wagner, F.R.; Armbrüster, M.; Kohout, M.; Leithe-Jasper, A.; Schwarz, U.; von Schnering, H.G. CuAl₂ revisited: Composition, crystal structure, chemical bonding, compressibility and Raman spectroscopy. *J. Solid State Chem.* **2006**, *179*, 1707–1719. [[CrossRef](#)]
36. Nishiyama, Z. *Martensitic Transformations*; Fine, M., Meshi, M., Wayman, C., Eds.; Academic Press: New York, NY, USA, 1978.
37. Cuenya, B.R.; Doi, M.; Löbus, S.; Courths, R.; Keune, W. Observation of the fcc-to-bcc Bain transformation in epitaxial Fe ultrafine films on Cu₃Au (001). *Surf. Sci.* **2001**, *493*, 338–360. [[CrossRef](#)]
38. Giannozzi, P.; Baroni, S.; Bonini, N.; Calandra, M.; Car, R.; Cavazzoni, C.; Ceresoli, D.; Chiarotti, G.L.; Cococcioni, M.; Dabo, I.; et al. QUANTUM ESPRESSO: A modular and open-source software project for quantum simulations of materials. *J. Phys. Condens. Matter* **2009**, *21*, 395502. [[CrossRef](#)] [[PubMed](#)]
39. Vanderbilt, D. Soft self-consistent pseudopotentials in a generalized eigenvalue formalism. *Phys. Rev. B* **1990**, *41*, 7892–7895. [[CrossRef](#)]
40. Perdew, J.P.; Burke, K.; Ernzerhof, M. Generalized gradient approximation made simple. *Phys. Rev. Lett.* **1996**, *77*, 3865–3868. [[CrossRef](#)] [[PubMed](#)]
41. Billeter, S.R.; Curioni, A.; Andreoni, W. Efficient linear scaling geometry optimization and transition-state search for direct wavefunction optimization schemes in density functional theory using a plane-wave basis. *Comput. Mater. Sci.* **2003**, *27*, 437–445. [[CrossRef](#)]
42. Parrinello, M.; Rahman, A. Crystal Structure and Pair Potentials: A Molecular-Dynamics Study. *Phys. Rev. Lett.* **1980**, *45*, 1196–1199. [[CrossRef](#)]
43. Baroni, S.; de Gironcoli, S.; Corso, A.D.; Giannozzi, P. Phonons and related crystal properties from density-functional perturbation theory. *Rev. Mod. Phys.* **2001**, *73*, 515–562. [[CrossRef](#)]
44. Phonopy. Available online: <http://atztogo.github.io/phonopy/> (accessed on 10 July 2019).
45. Golezorkhtabar, R.; Pavone, P.; Spitaler, J.; Puschnig, P.; Draxl, C. ElaStic: A tool for calculating second-order elastic constants from first-principles. *Comput. Phys. Commun.* **2013**, *184*, 1861–1873. [[CrossRef](#)]

46. Niu, H.; Niu, S.; Oganov, A.R. Simple and accurate model of fracture toughness of solids. *J. Appl. Phys.* **2019**, *125*, 065105. [CrossRef]
47. Stokes, H.T.; Hatch, D.M. ISOTROPY software package. Available online: <http://stokes.byu.edu/isotropy.html> (accessed on 10 June 2019).
48. Ivashchenko, V.I.; E A Turchi, P.; Gorb, L.; Leszczynski, J.; Medukh, N.R.; Shevchenko, R. Temperature-induced phase transitions in the rock-salt type SiC: A first-principles study. *J. Physics: Condens. Matter* **2019**, *31*, 405401. [CrossRef] [PubMed]
49. Kokalj, A. Computer graphics and graphical user interfaces as tools in simulations of matter at the atomic scale. *Comput. Mater. Sci.* **2003**, *28*, 155–168. [CrossRef]
50. Ivashchenko, V.I.; Turchi, P.E.A. Phonon softening and the phase transition in VN. *Phys. Rev. B* **2008**, *78*, 224113. [CrossRef]
51. Landesman, J.; Treglia, G.; Turchi, P.; Ducastelle, F. Electronic structure and pairwise interactions in substoichiometric transition metal carbides and nitrides. *J. Phys.* **1985**, *46*, 1001–1015. [CrossRef]
52. Ducastelle, F. Order and Stability in Alloys. In *Cohesion and Structure*; de Boer, F.R., Pettifor, D.G., Eds.; North-Holland Publishing Company: Amsterdam, The Netherlands; Oxford, UK; New York, NY, USA; Tokyo, Japan, 1991.
53. Bieber, A.; Ducastelle, F.; Gautier, F.; Tréglia, G.; Turchi, P. Electronic structure and relative stabilities of L12 and D022 ordered structures occurring in transition metal alloys. *Solid State Commun.* **1983**, *45*, 585–590. [CrossRef]
54. Kanamori, J. Magnetization process in an Ising system. *Prog. Theor. Phys.* **1966**, *35*, 16–35. [CrossRef]
55. Kaburagi, M.; Kanamori, J. A Method of Determining the Ground State of the Extended-Range Classical Lattice Gas Model. *Prog. Theor. Phys.* **1975**, *54*, 30–44. [CrossRef]
56. Villars, P.; Calvert, L.D. *Pearson's Handbook of Crystallographic Data for Intermetallic Phases*; American Society for Metals: Materials Park, OH, USA, 1985.
57. Kubaschewski, O. *Phase Diagrams of Binary Iron Alloys*; Okamoto, H., Ed.; ASM International: Materials Park, OH, USA, 1993; p. 380.
58. Hong, S.J.; Rhee, C.K.; Chun, B.S. Phase Transition and Thermoelectric Property of Ultra-fine Structured β -FeSi₂ Compounds. *Solid State Phenom.* **2006**, *118*, 591–596. [CrossRef]
59. Birkholz, C.; Schelm, J. Electrical investigation of the semi-conductor-to metal transition in FeSi₂. *Phys. Stat. Sol.* **1969**, *34*, K177–K180. [CrossRef]
60. Milekhinea, V.; Onsoienb, M.I.; Solberga, J.K.; Skaland, T. Mechanical properties of FeSi (ϵ), FeSi₂ (ζ_α) and Mg₂Si. *Intermetallics* **2002**, *10*, 743–750. [CrossRef]
61. Ravindran, P.; Fast, L.; Korzhavyi, P.A.; Johansson, B.; Wills, J.; Eriksson, O. Density functional theory for calculation of elastic properties of orthorhombic crystals: Application to TiSi₂. *J. Appl. Phys.* **1998**, *84*, 4891–4904. [CrossRef]
62. Krentsis, R.P.; Gel'd, P.V.S. Nauchn. Tr., Ural'sk. Preliminary Report on the Thermodynamic Properties of Selected Light-Element and Some Related Compounds. Available online: <https://books.google.rs/books?id=RTxRAAAAMAAJ&pg=PA423&pg=PA423&dq=Krentsis,+R.+P.;+Gel%25E2%2580%2599d,+P.+V.+Sb.+Nauchn.+Tr.,+Ural%25E2%2580%2599sk.+Politekhn&source=bl&ots=2-ij12RiZ2&sig=ACfU3U13Ju-1CNCu7rRV5AQOhD2mGvTzRQ&hl=en&sa=X&ved=2ahUKEwjW--LZoNyCAxWbgf0HHQprBDsQ6AF6BAGIEAM#v=onepage&q=Krentsis%252C%2520R.%2520P.%253B%2520Gel%25E2%2580%2599d%252C%2520P.%2520V.%2520Sb.%2520Nauchn.%2520Tr.%252C%2520Ural%25E2%2580%2599sk.%2520Politekhn&f=false> (accessed on 10 June 2019).
63. Maglic, K.; Parrot, J.E. Bundesministerium fur Bildung und Wissenschaft. *Forschungsbericht* **1970**, K70-01.

Disclaimer/Publisher's Note: The statements, opinions and data contained in all publications are solely those of the individual author(s) and contributor(s) and not of MDPI and/or the editor(s). MDPI and/or the editor(s) disclaim responsibility for any injury to people or property resulting from any ideas, methods, instructions or products referred to in the content.